Research Article – Vol. 02, Issue 03, No. 04

Advanced in Engineering and Intelligence Systems

Journal Web Page: https://aeis.bilijipub.com

Design and optimization of a Droop Controller to fix the frequency of a Microgrid System using the gray wolf algorithm with stability analysis

Zhi Yuan[1,1*], Ji Li [1,2]

[1] *Engineering Research Center of Renewable Energy Power Generation and Grid-connected Control, Ministry of Education, Xinjiang University, Urumqi, Xinjiang, 830017, China*
[2] *Electric Power Research Institute of State Grid Xinjiang Electric Power Co., Ltd., Urumqi, Xinjiang, 830011, China*

Highlights

- An optimal droop control strategy stabilizes grid frequency amid load disturbances.
- Gray wolf optimization optimizes microgrid parameters, including Droop control, for improved performance.
- Effective protection against frequency fluctuations caused by load changes.
- Comprehensive simulations demonstrate the proposed method's effectiveness in maintaining grid frequency stability during load disturbances.

Article Info

Received: 25 May 2023
Received in revised: 10 July 2023
Accepted: 16 July 2023
Available online: 30 September 2023

Keywords

Droop controller;
Microgrid;
Small-signal;
Model;
Gray wolf algorithms;
Optimization

Abstract

Switching between grid-connected and islanded mode and connection and broadcast performance in distributed resources and loads have recently raised many concerns. For this problem, Droop control is a very good solution. On the other hand, load changes cause dynamic and grid behavior disruptions, which requires an optimal control strategy to solve it. This paper presents an optimal droop control strategy to fix the grid frequency in the presence of consumer load disturbances. First, a small signal model is extracted for a microgrid in the presence of controllers, consumers, producers and other components. Then, using the gray wolf optimization algorithm, the parameters of the microgrid, including the Droop control parameters, are optimized. Finally, the whole closed-loop system is checked for stability in the presence of optimal parameters. The results show that the optimal control method presented in this article can protect the microgrid against frequency changes caused by load changes and fluctuations. The parameters and coefficients of the controllers of the desired control method in this article have been optimized to increase its performance as much as possible. To check the performance of the proposed method, a series of simulations are performed in the presence of load disturbances for the entire closed-loop system. The simulation results show the effective performance of the proposed optimal method, which can be used to keep the grid frequency stable in the presence of load disturbances.

* Corresponding Author: Zhi Yua
Email: yz22xju@163.com

1. Introduction

1.1. Field of study

The energy sector is entering an era where the primary increases in electrical energy demand will be supplied through the extensive installation of distributed generation (DG) as the energy crisis, and environmental pollution become increasingly serious recently. A cluster of DGs, controllers, energy storage devices, and loads comprise the independent control unit known as a microgrid, an advanced DGs operating regime [1], [2]. This regime can preserve grid dependability and address some issues brought on by massive DG access, making it a cutting-edge plan for future power supply and a crucial component of smart grid construction [3].

1.2.Literature

Microgrids can operate in grid-connected or autonomous modes, allowing unrestricted access to the utility grid [4]. However, because a microgrid has less physical inertia than conventional rotating machines [5], the dynamic response is significantly rapid, which makes the system susceptible to oscillation brought on by grid disruptions [6]. Small-signal stability is thus one of the key issues in the reliable operation of a microgrid. To keep power quality within the regulated range and improve dynamic performance, examining the small-signal model and choosing various controller or filter parameters is very important. The grid dynamics are typically ignored in conventional power systems' stability analyses, but in microgrids, the complexity and diversity of the DG's control strategy make it challenging to model the entire small-signal dynamic equation for microgrids. Small-signal modeling and microgrid performance analysis have subsequently evolved into a worrying challenge.

According to previous studies, the parameters of power sharing through root locus or sensitivity analysis and the microgrid's stability are closely related. According to reference [7], all of the small-signal model's sub-modules were developed in each inverter's local frame, and an examination of the system's eigenvalues revealed that the dominating low-frequency modes were extremely sensitive to the settings of the DG's power-sharing-controller. The model needs to be simplified for use in reality, though, as it is too complicated. The relationship between stability and influencing parameters like load droop gain and the equivalent line impedance was demonstrated in references [8], [9]. However, it did not present any particular optimization strategy; it merely obtained the regular pattern of parameter change. Reference [10] used particle swarm optimization to find optimal microgrid control parameter values. However, figuring out the search criteria and constraints is hard without considering the small-signal model. Reference [11] offered Particle Swarm Optimization (PSO) techniques for the droop controllers of inverter-interfaced DGs via dynamic model, but it only considered the influence of PI controller parameters; as a result, findings were incomplete and still required improvement.

Also, there are many different control strategies for microgrids, each with a small-signal model to represent steady-state and dynamic performance. Proper parameters will be chosen to achieve improved stability and dynamics by studying the small-signal model. Microgrid control in both modes may be divided into PQ control, V/f control, and droop control. According to references [12], [13], the droop control could be used in both modes to ensure that all DGs are in the same position and achieve a reasonable load distribution without communication. This prevented transient oscillation during the switch of operating modes and made it possible for DG's plug-and-play capabilities. To achieve equal power sharing and reduced circulating current, studies on droop management in both AC and DC microgrids have been done recently. In DC microgrids, several control techniques have been used, including the double-layer hierarchical control strategy [14], the adaptive droop control method based on the droop index [15], and the three-layer droop control approach [16]. To accomplish accurate power sharing, reference [17] suggested a unique droop control approach that considers the influence of complex impedance conditions. A virtual flux droop technique was developed by reference [18] to get lower frequency deviation. In [19], a small signal model is presented, and the obtained system analysis calculates the optimal parameters using the genetic algorithm. In reference [20], a sequential control based on V-I droop control for the energy management of microgrids has been performed. In reference [21], a two-stage droop control is designed for current sharing between DC-DC converters, maintaining asymptotic stability for local equilibrium points. In reference [22], a combination of PI controller and droop control is used for voltage-frequency control, and this control scheme is only limited to DC-type microgrids. In reference [23], a two-level structure for sharing active power and reactive power based on adaptive V-I droop control in microgrids is presented. The purpose of this structure is to eliminate voltage harmonics. In reference [24], a droop control for low-voltage microgrids based on AC power frequency is designed to improve load sharing and voltage characteristics. In reference [25], a new droop control is presented to synchronize and balance power in cascade-type microgrids.

1.3.Main contributions

This paper presents an optimal droop control strategy to fix the grid frequency in the presence of consumer load disturbances. First, a small signal model is extracted for a microgrid in the presence of controllers, consumers, producers, and other components. Then, using the gray wolf optimization algorithm, the parameters of the microgrid, including the Droop control parameters, are optimized. Finally, the whole closed-loop system is checked for stability in the presence of optimal parameters.

The results show that the optimal control method presented in this article can protect the microgrid against frequency changes caused by load changes and fluctuations. The parameters and coefficients of the controllers of the desired control method in this article have been optimized to increase its performance as much as possible.

1.4.Paper organization

The rest of this paper is structured as follows. A typical microgrid construction based on droop control is shown in Section 2. The modeling of the inverter, grid, and load is discussed in Section 3 and get a comprehensive microgrid small-signal equation. The optimization objective function and GWA optimization technique during the dynamic switching process are proposed in Section 4. Results from a Simulink evaluation are presented in Section 5 to show how well the suggested small-signal model and optimization strategy work. In Section 6, conclusions are presented.

2. Droop control-based microgrid system

Using the linear droop characteristic of frequency to active power (f - P) and voltage magnitude to reactive power (u - Q), droop management can accurately share power amongst many DGs to balance abrupt disruptions, mimicking the governor concept of a traditional synchronous generator. Three loops comprise the controller: 1) Power-sharing control is used to adjust the fundamental voltage of the inverter's frequency and magnitude by the droop coefficients. 2) Voltage control produces close control of the output voltage and synthesizes the reference current vector. 3) Inner current control is used to react to the filter-inductor current quickly, reject high-frequency disturbances, and generate voltage vector signals for the Pulse-Width Modulation (PWM) module [26].

Figure 1 is a typical microgrid that is addressed in this paper. Because most energy sources, including wind and solar, may be regarded as DC sources after rectification, it has two DGs are presumed to be DC sources. Each DG first connects a local static load using a three-leg inverter, LC filters L_f and C_f, and coupling inductors L_c. Next, each DG connects to the AC bus with common load using line impedance $R_{line}$and L_{line}. The microgrid will run in autonomous mode when the Point of Common Coupling (PCC) that connects the AC bus and utility grid is deactivated.

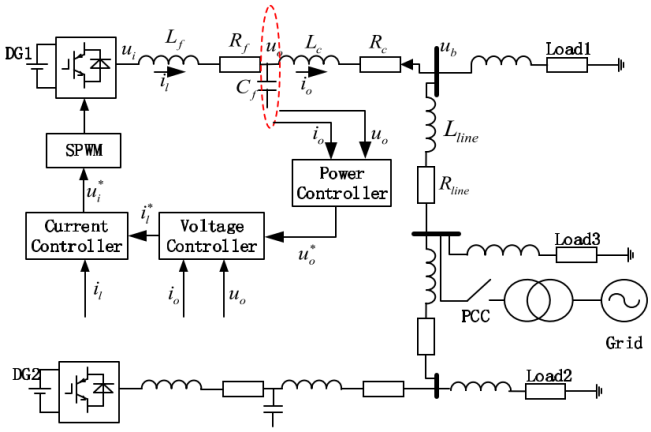

Fig. 1. Equivalent circuit and control structure for a microgrid.

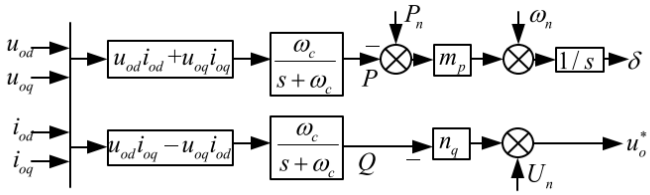

Fig. 2. Power controller block diagram

3. Microgrid small-signal modeling

This section analyses and formulates mathematical equations for the microgrid depicted as blocks in Figure 1. To create the small-signal model and analyze the system's stability, these equations must be linearized around an operational point because they are nonlinear.

Paralleled inverters, the grid, and the loads comprise the three main sub-modules of the small-signal dynamic model of the entire microgrid system [27]. Before combining them to create the model of the entire system, the small-signal model of the submodules is first separately constructed.

3.1.Droop-Controlled Inverters and Interface Circuit

Often, a voltage-source three-phase bridge inverter (VSI), an output LC filter, and a coupling inductor connect DG units to the microgrid grid. Ignoring the impact of its high switching frequency, the Power-sharing controller, voltage and current closed-loop controller are the three components of the droop controller of a VSI. Each

component's dynamic model is derived in the manners listed below.

1) Power Controller Modeling: According to Figure 2., the fundamental concept behind power sharing is to balance any load increase by reducing the system's frequency and voltage amplitude by droop characteristics.

Using the two-axis theory, the observed output voltage and current determine the instantaneous active and reactive power. The average powers corresponding to the basic component are derived using a low-pass filter to produce excellent power quality:

$$\begin{cases} \dot{\Delta P} = -\omega_c \Delta P + \omega_c \left(I_{od} \Delta u_{od} + I_{oq} \Delta u_{oq} + U_{od} \Delta i_{od} + U_{oq} \Delta i_{oq} \right) \\ \dot{\Delta Q} = -\omega_c \Delta Q + \omega_c \left(I_{oq} \Delta u_{od} - I_{od} \Delta u_{oq} - U_{oq} \Delta i_{od} + U_{od} \Delta i_{oq} \right) \end{cases} \tag{2}$$

The fundamental voltage and frequency of a paralleled inverter system are set by the droop gain, which is defined as:

$$\begin{cases} \omega = \omega_n - m_p (P - P_n) \\ u_{od}^* = U_n - n_q Q \\ u_{oq}^* = 0 \end{cases} \tag{3}$$

where the static droop gains are m_p and n_q. The following are the two-axis small-signal models for frequency and voltage:

$$\begin{cases} \Delta\omega = -m_p (\Delta P) \\ \Delta u_{od}^* = -n_q \Delta Q \\ \Delta u_{oq}^* = 0 \end{cases} \tag{4}$$

The angle difference between the d-q frames of each inverter and the common D-Q frame is defined as follows to transform all the variables from each inverter reference to a common frame:

$$\delta = \int (\omega - \omega_{com}) dt \tag{5}$$

The common frame's angular frequency is ω_{com} which is often obtained by the first inverter. This is the small-signal model:

$$\Delta\dot{\delta} = \Delta\omega - \Delta\omega_{com} = -m_p (\Delta P) - \Delta\omega_{com} \tag{6}$$

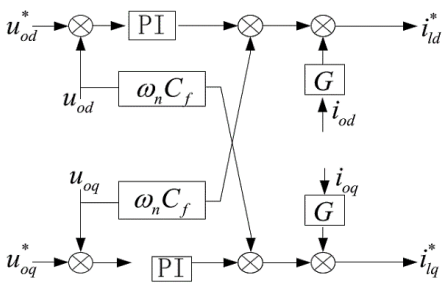

Fig. 3. Voltage controller's block diagram.

2) Voltage Controller Model: The voltage control loop uses a typical proportional and integral (PI) regulator

$$\begin{cases} P = \dfrac{\omega_c}{s + \omega_c} (u_{od} i_{od} + u_{oq} i_{oq}) \\ Q = \dfrac{\omega_c}{s + \omega_c} (u_{od} i_{oq} + u_{oq} i_{od}) \end{cases} \tag{1}$$

where s is the Laplace transform factor; u_{od}, u_{od}, i_{od}, and i_{oq} are the output voltages and currents in the dq reference frame; and ω_c is the low-pass filter's cut-off frequency. As a result, the following gives the small-signal dynamic model of power control:

to generate the reference decoupling current vector as shown in Figure 3. It compares the sampled output voltage with the reference value provided by the power controller, obtains a feed-forward gain to compensate for output current disturbances, and outputs the reference decoupling current vector.

The associated state equations are as follows:

$$\begin{cases} \dfrac{d\emptyset_d}{dt} = (u_{od}^* - u_{od}) \\ \dfrac{d\emptyset_q}{dt} = (u_{oq}^* - u_{oq}) \end{cases} \tag{7}$$

$$\begin{cases} i_{ld}^* = K_{iu} \emptyset_d + K_{pu} (u_{od}^* - u_{od}) - \omega_n C_f u_{oq} + G i_{od} \\ i_{lq}^* = K_{iu} \emptyset_q + K_{pu} (u_{oq}^* - u_{oq}) + \omega_n C_f u_{od} + G i_{oq} \end{cases} \tag{8}$$

where K_{pu} and K_{iu} represent the proportional and integral voltage gains respectively; C_f is the LC filter's per-phase capacitance. G is the feed-forward control gain. The voltage control small-signal model can be presented by:

$$\begin{cases} \Delta\dot{\emptyset}_d = \Delta u_{od}^* - \Delta u_{od} \\ \Delta\dot{\emptyset}_q = \Delta u_{oq}^* - \Delta u_{oq} \end{cases} \tag{9}$$

$$\begin{cases} \Delta i_{ld}^* = K_{iu} \Delta\emptyset_d + K_{pu} \Delta u_{od}^* - K_{pu} \Delta u_{od} - \omega_n C_f \Delta u_{oq} + \\ \Delta i_{lq}^* = K_{iu} \Delta\emptyset_q + K_{pu} \Delta u_{oq}^* + \omega_n C_f \Delta u_{od} - K_{pu} \Delta u_{oq} + \end{cases} \tag{10}$$

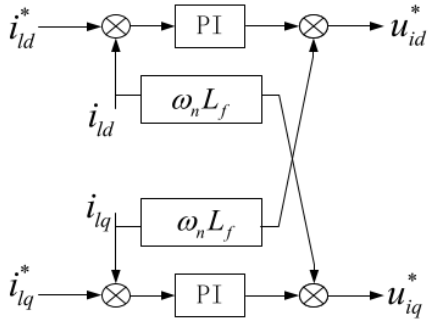

Fig. 4. Current controller's block diagram.

3) Current Controller Model: Like the voltage control loop, the current controller produces the SPWM signal with the least amount of current error by comparing the reference value provided by the voltage controller to the current sampled filter current by using a PI controller, as illustrated in Figure 4. The voltage control small-signal model is:

$$\begin{cases}\Delta\dot{\gamma}_d = \Delta i_{ld}^* - \Delta i_{ld} \\ \Delta\dot{\gamma}_q = \Delta i_{lq}^* - \Delta i_{lq}\end{cases} \tag{11}$$

$$\begin{cases}\Delta u_{ld}^* = K_{ic}\Delta\gamma_d + K_{pu}\Delta i_{ld}^* - K_{pc}\Delta i_{ld}) - \omega_n L_f \Delta i_{lq} \\ \Delta u_{lq}^* = K_{ic}\Delta\gamma_q + K_{pc}\Delta i_{lq}^* + \omega_n L_f \Delta i_{ld} - K_{pc}\Delta i_{lq})\end{cases} \tag{12}$$

where L_f is the per-phase inductance, i_{ld}, i_{lq} are the filter currents in the dq reference frame, and K_{pc}, K_{ic} are the proportional and integral gains of current, respectively.

4) LC Filter and Coupling Inductance Model: The inverter connected to the grid may eliminate the harmonic wave close to the switching frequency with the LC filter and coupled inductor. The small-signal linearized model is:

$$\begin{cases}\dot{\Delta i}_{ld} = -\frac{R_f}{L_f}\Delta i_{ld} + \omega_o \Delta i_{iq} - \frac{1}{L_f}\Delta u_{od} + \frac{1}{L_f}\Delta u_{id} + I_{lq}\Delta\omega \\ \dot{\Delta i}_{lq} = -\omega_o \Delta i_{ld} - \frac{R_f}{L_f}\Delta i_{lq} - \frac{1}{L_f}\Delta u_{oq} + \frac{1}{L_f}\Delta u_{iq} - I_{ld}\Delta\omega\end{cases} \tag{13}$$

$$\begin{cases}\Delta\dot{u}_{od} = \frac{1}{C_f}\Delta i_{ld} + \omega_o \Delta u_{oq} - \frac{1}{C_f}\Delta i_{od} + U_{oq}\Delta\omega \\ \Delta\dot{u}_{oq} = \frac{1}{C_f}\Delta i_{lq} - \omega_o \Delta i_{lq} - \frac{1}{C_f}\Delta i_{oq} - U_{od}\Delta\omega\end{cases} \tag{14}$$

$$\begin{cases}\dot{\Delta i}_{od} = \frac{1}{L_c}\Delta u_{od} - \frac{R_c}{L_c}\Delta i_{od} + \omega_o \Delta i_{oq} - \frac{1}{L_c}\Delta u_{bd} + I_{oq}\Delta\omega \\ \dot{\Delta i}_{oq} = \frac{1}{L_c}\Delta u_{oq} - \omega_o \Delta i_{od} - \frac{R_c}{L_c}\Delta i_{oq} - \frac{1}{L_c}\Delta u_{bq} - I_{od}\Delta\omega\end{cases} \tag{15}$$

where the dq axis bus voltages are u_{bd} and u_{bq}; The inverter voltages in the dq frame are $u_{id}$and u_{iq}, respectively. At the initial operating point, the steady-state values are ω_o, I_{ld}, I_{lq}, U_{od}, U_{oq}, I_{od}, and I_{oq}.

$$[\Delta x_{INVI}] = A_{INV}[\Delta x_{INV}] + B_{INV}[\Delta u_{bDQ}]$$
$$[\Delta i_{oDQ}] = C_{INVc}[\Delta x_{INV}]$$

where:

$[\Delta x_{INV}]=[\Delta x_{inv1}\ \Delta x_{inv2}]^T$ $[\Delta u_{bDQ}]=[\Delta u_{bDQ1}\ \Delta u_{bDQ2}]^T$;

$$A_{INV} = \begin{bmatrix}A_{INV1} + B_{1\omega com}C_{INV\omega 1} & \\ B_{2\omega com}C_{INV\omega 1} & A_{INV2}\end{bmatrix}; B_{INV} = \begin{bmatrix}B_{INV1} & \\ & B_{INV2}\end{bmatrix};$$

$$C_{INVc} = \begin{bmatrix}C_{INVc1} & \\ & C_{INVc2}\end{bmatrix}$$

5) Complete Model of the DG Interface: Using the transformation matrix shown below, output variables i_{oDQ} and input variables u_{bdq} may be converted to the common DQ frame:

$$[i_{oDQ}] = [T][i_{odq}] = \begin{bmatrix}\cos(\delta) & -\sin(\delta) \\ \sin(\delta & \cos(\delta)\end{bmatrix}[i_{odq}] \tag{16}$$

$$[U_{bdq}] = [T^{-1}][u_{bDQ}] = \begin{bmatrix}\cos(\delta) & \sin(\delta) \\ -\sin(\delta & \cos(\delta)\end{bmatrix}[u_{bDQ}] \tag{17}$$

Linearizing the previous formula:

$$\begin{aligned}&[\Delta i_{oDQ}] \\ &= \begin{bmatrix}\cos(\delta) & -\sin(\delta) \\ \sin(\delta & \cos(\delta)\end{bmatrix}[\Delta i_{odq}] \\ &+ \begin{bmatrix}-I_{od}\sin(\delta_o) - I_{oq}\cos(\delta_o) \\ I_{od}\cos(\delta_o) - I_{oq}\sin(\delta_o)\end{bmatrix}[\Delta\delta]\end{aligned} \tag{18}$$

$$\begin{aligned}&[\Delta u_{bdq}] \\ &= \begin{bmatrix}\cos(\delta_o) & \sin(\delta_o) \\ -\sin(\delta_o) & \cos(\delta_o)\end{bmatrix}[\Delta u_{bDQ}] \\ &+ \begin{bmatrix}-U_{bD}\sin(\delta_o) - U_{bQ}\cos(\delta_o) \\ U_{bD}\cos(\delta_o) - U_{bD}\sin(\delta_o)\end{bmatrix}[\Delta\delta]\end{aligned} \tag{19}$$

A full 13-order small-signal state space equation and output equation of a single inverter unit in the common frame may be derived as follows, which can be a conventional inverter model, by combining the state-space models presented in Equations (2) – (19), selecting the following thirteen state variables.

$$[\Delta\dot{x}_{invi}] = A_{INVi}[\Delta x_{invi}] + B_{INVi}[\Delta u_{bDQi}] + B_{i\omega com}[\Delta\omega_{com}] \tag{20}$$

$$\begin{bmatrix}\Delta\omega_i \\ \Delta i_{oDQi}\end{bmatrix} = \begin{bmatrix}C_{INV\omega i} \\ C_{INVci}\end{bmatrix}[\Delta x_{invi}] \tag{21}$$

as shown at the top of the next page, where

$[\Delta x_{invi}] =$
$[\Delta\delta_i\ \Delta P_i\ \Delta Q_i\ \ \Delta\emptyset_{di}\ \ \Delta\emptyset_{qi}\ \Delta\gamma_{di}\ \ \Delta\gamma_{qi}\ \ \Delta i_{ldi}\ \Delta_{lqi}\ \Delta u_{odi}\ \Delta u_{oqi}\ \Delta i_{odi}\ \Delta i_{oqi}]^T$
.

6) Combined Model of Two Parallel Inverters: For the small-signal model for two parallel inverters depicted in Figure 1, which is based on the individual inverter models in (20) and (21), the following can be deduced:

$$[\Delta x_{INVI}] = A_{INV}[\Delta x_{INV}] + B_{INV}[\Delta u_{bDQ}]$$
$$[\Delta i_{oDQ}] = C_{INVc}[\Delta x_{INV}] \tag{22}$$

$$A_{INVi} = \begin{bmatrix} 0 & -m_p & & & & & & & & & & \\ 0 & -\omega_c & & & & & & & \omega_c I_{od} & \omega_c I_{oq} & \omega_c U_{od} & \omega_c U_{oq} \\ 0 & 0 & -\omega_c & & & & & & \omega_c I_{oq} & -\omega_c I_{od} & -\omega_c U_{oq} & \omega_c U_{od} \\ 0 & 0 & -n_q & & & & & & -1 & 0 & 0 & 0 \\ 0 & 0 & 0 & & & & & & 0 & -1 & 0 & 0 \\ 0 & 0 & -n_q K_{Pu} & K_{iu} & & & -1 & & -K_{Pu} & -\omega_n C_f & G & 0 \\ 0 & 0 & 0 & 0 & K_{iu} & & 0 & -1 & \omega_n C_f & -K_{Pu} & 0 & G \\ 0 & -m_p I_{lq} & \frac{-n_q K_{Pu} K_{Pc}}{L_f} & \frac{K_{iu} K_{Pc}}{L_f} & 0 & \frac{K_{ic}}{L_f} & \frac{-K_{Pc} - R_f}{L_f} & \omega_o - \omega_n & \frac{-K_{Pu} K_{Pc} - 1}{L_f} & -\frac{\omega_n C_f K_{Pc}}{L_f} & \frac{K_{Pc} G}{L_f} & 0 \\ 0 & m_p I_{ld} & & & \frac{K_{iu} K_{Pc}}{L_f} & 0 & \frac{K_{ic}}{L_f} & \omega_n - \omega_o & \frac{-K_{Pc} - R_f}{L_f} & \frac{\omega_n C_f K_{Pc}}{L_f} & \frac{-K_{Pu} K_{Pc} - 1}{L_f} & 0 & \frac{K_{Pc} G}{L_f} \\ 0 & -m_p U_{oq} & & & & & C_f^{-1} & 0 & 0 & \omega_o & -C_f^{-1} & 0 \\ 0 & m_p U_{od} & & & & & & C_f^{-1} & -\omega_o & 0 & 0 & -C_f^{-1} \\ \frac{U_{bD}\sin\delta_0 - U_{bQ}\cos\delta_0}{L_c} & -m_p I_{oq} & & & & & & & L_c^{-1} & 0 & -\frac{R_c}{L_c} & \omega_o \\ \frac{U_{bD}\cos\delta_0 + U_{bQ}\sin\delta}{L_c} & m_p I_{od} & & & & & & & & L_c^{-1} & -\omega_o & -\frac{R_c}{L_c} \end{bmatrix}$$

$$B_{IiVi} = \begin{bmatrix} 0 & \cdots & 0 & -\frac{\cos(\delta_o)}{L_c} & -\frac{\sin(\delta_o)}{L_c} \\ 0 & \cdots & 0 & \frac{\sin(\delta_o)}{L_c} & -\frac{\cos(\delta_o)}{L_c} \end{bmatrix}^T_{2\times 13}; \quad B_{i\omega com} = [-1\ 0\ \ldots\ 0]^T_{1\times 13};$$

$$C_{INV\omega i} = \begin{cases} [0\ -m_p\ 0\ \ldots\ 0]_{l\times 13} & i = 1 \\ [0 \ldots 0]_{1\times 13} & i \neq 1 \end{cases};$$

$$C_{INVci} = \begin{bmatrix} -I_{od}\sin\delta_o - I_{oq}\cos\delta_o & 0 & \ldots & 0 & \cos\delta_o & -\sin\delta_o \\ I_{od}\cos\delta_o - I_{oq}\sin\delta_o & 0 & \ldots & 0 & \sin\delta_o & \cos\delta_o \end{bmatrix}_{2\times 13}$$

It can be seen that the state matrix model A_{INV} is distinct from the parallel model suggested in [8] as demonstrated in (23). Each inverter is modeled in [8] using its different reference frame. However, one of the individual inverters' reference frames describes the state equations of the grid and the loads. This frame of reference is regarded as the standard reference frame. In this instance, it is necessary to convert the other inverters to this standard reference frame. The common angular frequency of the entire system, or $\Delta\omega_{com}$=$\Delta\omega_1$=$C_{INV\omega 1}\,\Delta x_{inv1}$, is chosen in this study to be the output angular frequency of the first inverter. As a result, it is simpler to create the state matrix since the transformation effort is substantially avoided. The coupling items in the state matrix model A_{INV} described in (22) are clearer and more precise in describing the specific impacts that the state variables of the common inverter have on the other inverters. Meanwhile, the new model's A_{INV} no longer requires the computation of $C_{INV\omega 2}$, considerably reducing the amount of calculation, particularly in the microgrid with several DGs.

$$A_{INV} = \begin{bmatrix} A_{INVI} + B_{1\omega com} C_{INV\omega 1} & 0 \\ 0 & A_{INV2} + B_{2\omega com} C_{INV\omega 2} \end{bmatrix} \quad (23)$$

3.2. Load and Grid Model

The LC filter linearization procedure may be used to construct the small-signal grid model for the microgrid seen in Fi. 1, resulting in the following model in the DQ frame:

$$[\Delta\dot{i}_{lineDQ}] = A_{NET}[\Delta i_{lineDQ}] + B_{INET}[\Delta u_{bDQ}] + B_{2NET}\Delta\omega \quad (24)$$

$$[\Delta\dot{i}_{loadDQ}] = A_{LOAD}[\Delta i_{loadDQ}] + B_{1LOAD}[\Delta u_{bDQ}] + B_{2LOAD}\Delta\omega \quad (25)$$

where:

$$A_{NET} = \begin{bmatrix} -\frac{R_{line1}}{L_{line1}} & \omega_0 & & \\ -\omega_0 & -\frac{R_{line1}}{L_{line1}} & & \\ & & -\frac{R_{line2}}{L_{line2}} & \omega_0 \\ & & -\omega_0 & -\frac{R_{line2}}{L_{line2}} \end{bmatrix}$$

$$B_{1NET} = \begin{bmatrix} \frac{1}{L_{line1}} & -\frac{1}{L_{line1}} & & \\ \frac{1}{L_{line1}} & -\frac{1}{L_{line1}} & & \\ & & \frac{1}{L_{line2}} & -\frac{1}{L_{line2}} \\ & & \frac{1}{L_{line2}} & -\frac{1}{L_{line2}} \end{bmatrix}$$

It is not addressed here since the coefficient matrix of the

load model is nearly identical to that of the grid model above.

3.3. Complete Microgrid Model

To adequately describe the input variables u_{bDQ}, a big enough virtual resistor r_N is assumed between each node and ground, which can lessen the influence on dynamic stability of the system. The small-signal model of the node is provided by:

$$[\Delta u_{bDQ}] = R_N(M_{INV}[\Delta i_{oDQ}] + M_{LOAD}[\Delta i_{loadDQ}] + M_{NET}[\Delta i_{lineDQ}] \quad (26)$$

where M_{INV} maps DG connection points onto micro-grid grid nodes, M_{LOAD} maps load connection points onto nodes, and M_{NET} maps connecting lines onto nodes. In Figure 1, there are s=2 DG, n=2 lines, p=3 loads, and m=3 nodes, so:

$$downrightR_N = \begin{bmatrix} r_N & & \\ & \ddots & \\ & & r_N \end{bmatrix} 2m \times 2m$$

$$M_{INV} = \begin{bmatrix} 1 & & & & & \\ & 1 & & & & \\ & & 0 & 0 & 0 & 0 \\ & & 0 & 0 & 0 & 0 \\ & & & & 1 & \\ & & & & & 1 \end{bmatrix}_{2m \times 2s}$$

$$M_{LOAD} = \begin{bmatrix} -1 & & \\ & \ddots & \\ & & 1 \end{bmatrix} 2m \times 2p$$

$$M_{NET} = \begin{bmatrix} -1 & \\ 0 & -1 \\ 1 & 0 & -1 \\ 1 & 0 & -1 \\ & 1 & 0 \\ & & 1 \end{bmatrix}_{2m \times 2n}$$

The entire full (2n + 2p + 13s) = 36 order small-signal model of Figure 1 is obtained based on Equations (22)–(26):

$$\begin{bmatrix} \Delta\dot{x}_{INV} \\ \Delta\dot{i}_{IlineDQ} \\ \Delta\dot{i}_{loadDQ} \end{bmatrix} = A_{sys} \begin{bmatrix} \Delta x_{INV} \\ \Delta i_{IlineDQ} \\ \Delta i_{loadDQ} \end{bmatrix} \quad (27)$$

where:

$$operation\ and\ economic\ factors\ after\ placement\ illustrates A_{sys} = \begin{bmatrix} A_{INV} + B_{INV}R_NM_{INV}C_{INVc} & B_{INV}R_NM_{NET} & B_{INV}R_NM_{LOAD} \\ B_{1NET}R_NM_{INV}C_{INVc} + B_{2NET}C_{INV\omega} & A_{NET}+B_{1NET}R_NM_{NET} & B_{INET}R_NM_{LOAD} \\ B_{1LOAD}R_NM_{INV}C_{INVc} + B_{2LOAD}C_{INV\omega} & B_{1LOAD}R_NM_{NET} & A_{LOAD}+B_{1LOAD}R_NM_{LOAD} \end{bmatrix}$$

4. Microgrid control and optimization based on the gray wolf algorithm

Since a microgrid can transition between grid-connected and islanded states, a workable objective function guarantees the stability and smooth switching of the various operating modes. Given that DG output power is a key indicator of system performance, the integral of deviation between instantaneous power and nominal power can be used in various operation modes under disturbances as the optimization objective function to represent dynamic performance, and try to minimize the integral value, which means the power can respond quickly to changes in nominal power and be stabilized without experiencing significant overshoot during the switching. The objective function is best described as follows:

$$minJ = \sum_{i=1}^{M} \left\{ \int_{t=t_0^i}^{t_f^i} (t - t_0^i)[P(t) - P^*(t))^2 + (Q(t) - Q^*(t))^2]dt \right. \quad (28)$$

where t_0^i, t_f^i are the start and end times for operation mode i, and M is the number of operation modes for the microgrid.

The problem cannot be solved using conventional mathematical optimization techniques because the objective function is not differentiable. The improved gray wolf algorithm (IGWO) accelerates the convergence and improves the accuracy of GWO optimization with an evolution and constraint mechanism to achieve a balance between exploration and exploitation. Biological evolution and the principle of "survival of the fittest" (SOF) have been added to the original gray wolf algorithm. A differential evolutionary algorithm (DEA) has been used as the evolutionary model of wolves. The wolf pack is updated according to the SOF principle, so the algorithm does not reach the local optimum. After each repetition of the algorithm, sort the fit value of each wolf in ascending order and then remove R wolves with the worst fit value. Meanwhile, randomly generate new wolves equal to the number of wolves removed [28].

In nature, organisms continuously evolve from low to advanced levels under the influence of heredity, selection, and mutation. Likewise, there are a series of changes, such as heredity, selection, and mutation, in the search process of wolves. Based on nature's biological evolution, methods such as differential evolution (DE), quantum evolution, cooperative evolution, etc., have been developed. The simple differential evolutionary strategy has fewer parameters, is easy to implement, and has been widely researched and used. Therefore, the DE strategy is chosen for the evolution of GWO. The basic principle of the DE

operator is to take the difference between individuals to recombine the population, obtain the middle individuals, and then obtain the next generation population. This strategy must include three operations: mutation, cutting, and selection.

The most obvious feature of differential evolution is the mutation operation. When an individual is selected, two weighted differences are added to the individual to make the difference. The main element of DE change is the parental difference vector, and each vector contains two different individuals (x_{r1}^t, x_{r2}^t) from the parents (generation t).

$$Dd_{r12} = x_{r1}^t - x_{r2}^t \tag{29}$$

where, $r1$ and $r2$ express the index number of two different people from the population. The mutation operation can be described as follows:

$$V_i^{t+1} = x_{r3}^t + F * (x_{r1}^t - x_{r2}^t) \tag{30}$$

$r1$, $r2$ and $r3$ are different integers in the range (1, 2, . . . n) of the index of the current target vector i. F is the scaling factor to control the scaling of the differential vector. In this method, the outstanding wolves are selected as parents to produce the ideal variety and ensure they can evolve in operation. Economic factors illustrate simulation trials after placement. Beta and delta are selected as parents and combined with alpha.

$$V_i^{t+1} = x_\alpha^t + F * (x_\beta^t - x_\delta^t) \tag{31}$$

In the first stage, a dynamic scaling factor is used to prevent the algorithm from falling into the local optimum, and in the second stage, a dynamic scaling factor is used to have a high exploitation ability to increase the speed of convergence. Therefore, the scaling factor F changes from large to small according to the number of repetitions in the equation.

For the target vector of wolves x_i^t, the cutting operation is performed with the change vector V_i^{t+1}, and the test vector U_i^{t+1} is produced. IToguarantee the evolution of x_i^t, a random selection method is adopted. For the other bits of U_i^{t+1}, the cutting probability coefficient CR is used to decide which bit of U_i^{t+1} is represented by V_i^{t+1} and which bit is represented by x_i^t.

$$U_{ij}^{t+1} = \begin{cases} V_{ij}^{t+1} \; rand(j) \le CR \; or \; j = rand(i) \\ x_{ij} \; rand(j) \ge CR \; and \; j \ne rand(i) \end{cases} j = 1,2,\dots,D \tag{32}$$

The "greedy selection" strategy is applied to the selection operation. After mutation operation and cutting operation, experimental individual U_i^{t+1} is produced to compete with x_i^t.

$$x_i^{t+1} = \begin{cases} U_i^{t+1} \; f(U_i^{t+1}) < f(x_i^t) \\ x_i^t \; f(U_i^{t+1}) \ge f(x_i^t) \end{cases} i = 1,2,\dots,n \tag{33}$$

In the wild, some vulnerable wolves will be eliminated due to an uneven distribution of prey, starvation, disease, and other reasons. Meanwhile, new wolves will join this wolf organization to strengthen it. Suppose the number of wolves in the group is fixed, and their fitness value measures the strength of the wolves. The higher the fit, the better the solution. Therefore, after each iteration of the algorithm, sort the fitness value of each wolf in ascending order and then remove the R wolves with the larger fitness values. Meanwhile, they randomly generate new wolves equal to the number of wolves removed. When R is large, the number of wolves that produce new ones is high, which helps to increase the diversity of wolves. But if the value of R is too large, the algorithm tends towards random search, which leads to slow convergence speed. If the value of R is too small, it is unsuitable for maintaining population diversity. Therefore, R is a random integer between $\frac{n}{2\varepsilon}$ and $\frac{n}{\varepsilon}$. The flowchart of the proposed algorithm is shown in Figure 5:

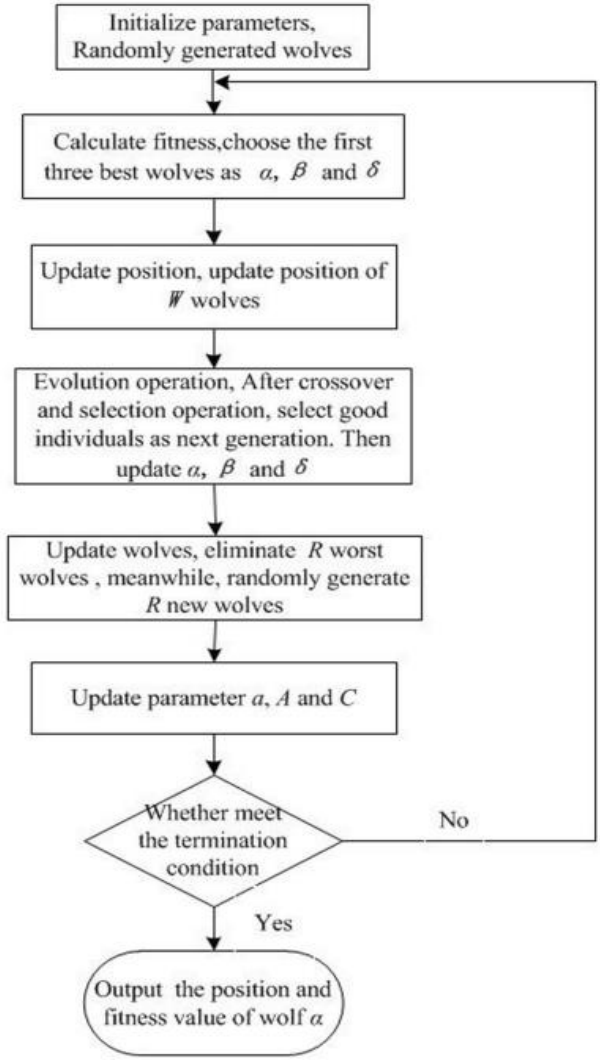

Fig. 5. The optimal gray wolf flowchart in the proposed method.

5. Simulation results

5.1. Performance validation

In this section, the results of the validation and the results of the microgrid are stated. Considering that the modeled microgrid should be stable and its frequency, which is 60 Hz, should not change due to load changes, the controller parameters and other parameters should be determined optimally. Also, to display the sudden change in load, in the interval [0. 9 0.75], The load size changes in the consumer, which is indicated by the frequency value display, which remains at 60 Hz.

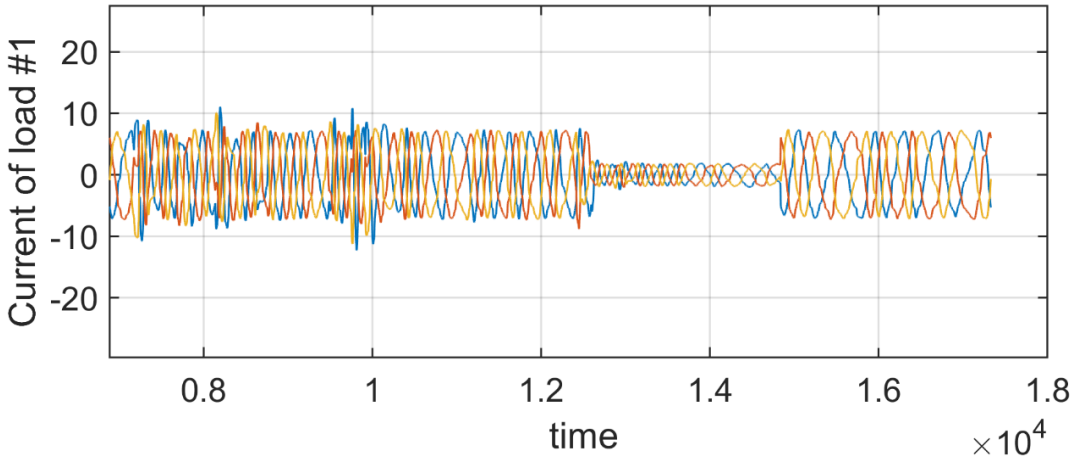

Fig. 6. Load current

Figure 6 shows the microgrid load flow. In this figure, it can be seen that with the change of the voltage, the load current decreases and then the load current returns to its previous state, which shows the validity of the modeling. In other words, to measure the performance of the desired drop control system against changes in the load of consumers, the amount of load has been changed at times to determine whether the desired control system is able tcan grid frequency constant in the presence of changes in load.

Figure 7 shows the amount of load frequency changes. According to the load flow variation shown in Figure 5, the amount of load changes is proportional to its change, which is evident in Figure 7. The point is that the purpose of the control loops in this simulation is to keep the frequency of the load constant despite the sudden changes in the load. Figure 6 shows the performance of the control method well, and the frequency changes proportional to the load changes remain constant.

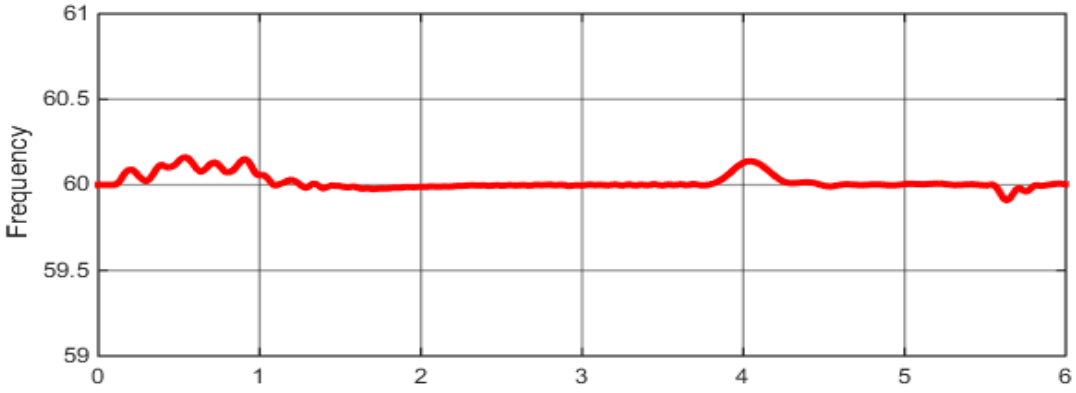

Fig.7. Frequency

As shown in Figure 7, the frequency during the simulation was kept close to 60 Hz with an acceptable error, which is the same as the grid frequency, and this indicates that the load changes, due to the presence of the mentioned controllers, did not change the frequency. Figures. 8 and 9 also show the graph of power changes (positive sequence) and phasor power of consumer number 1.

According to Figure 8, which shows the grid power changes, it can be seen that the amount of power changes (positive sequence) is consistent with the current change. Also, according to Figure 9, where the power (phasor) is

shown, it can be seen that this number of changes is based on the positive sequence power changes. Figure 10 shows the output voltage diagram of the inverter. According to Figure 10, it can be seen that the output voltage of the inverter changes in a specific range (250, -250), which indicates the optimal performance of the grid, and the grid does not operate outside the specified range.

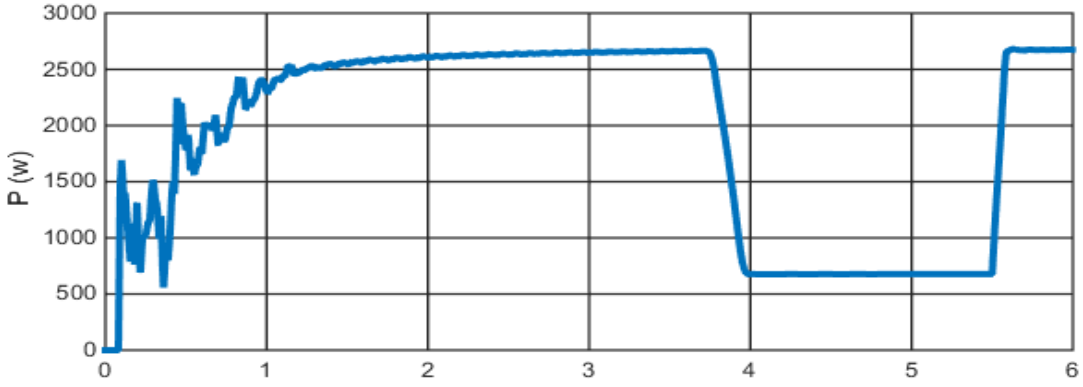

Fig.8. Grid power changes

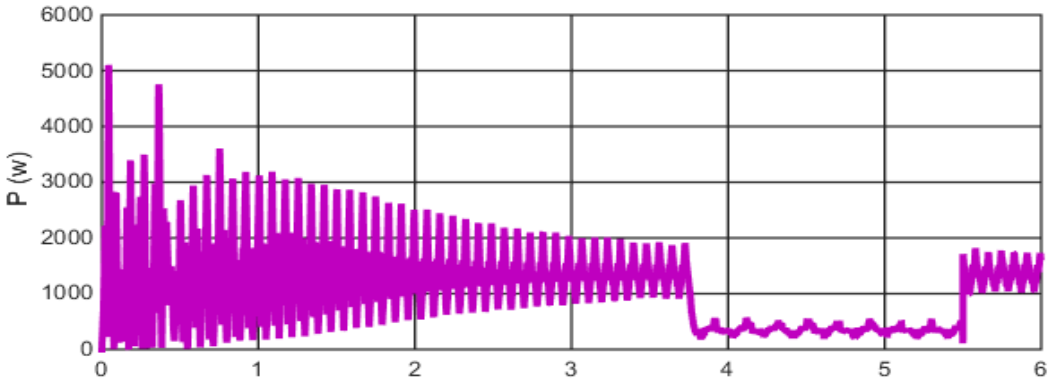

Fig.9. Positive sequence of power

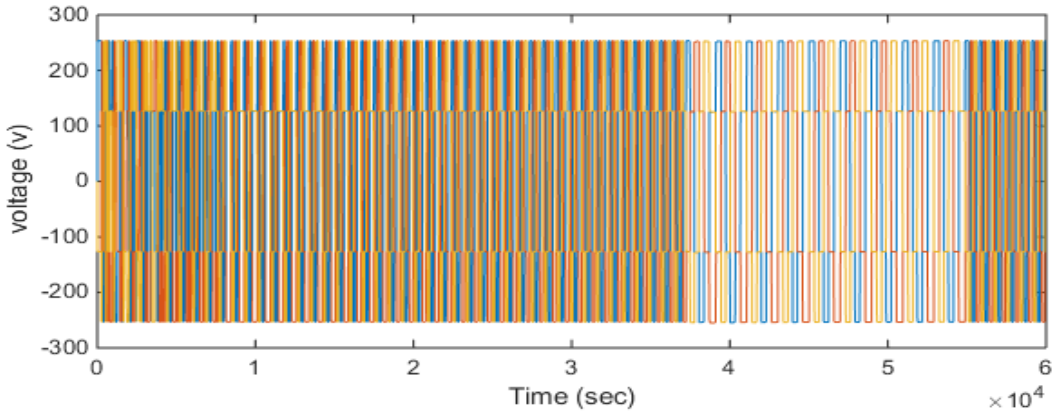

Fig.10. Output voltage diagram

Figures 11 and 12 show the line voltage and current diagrams after the filter. According to the figures, it can be seen that the number of changes in the current after the filter is also within a certain range and with the change in the current structure, the amount of line voltage and line current after the filter also changes accordingly and within the specified range of voltage and current in the grid is created It should be noted that the horizontal axis is based on sample time. As can be seen from the figures, the frequency has decreased slightly during the load change, and the controllers have been able to return the frequency to the reference level.

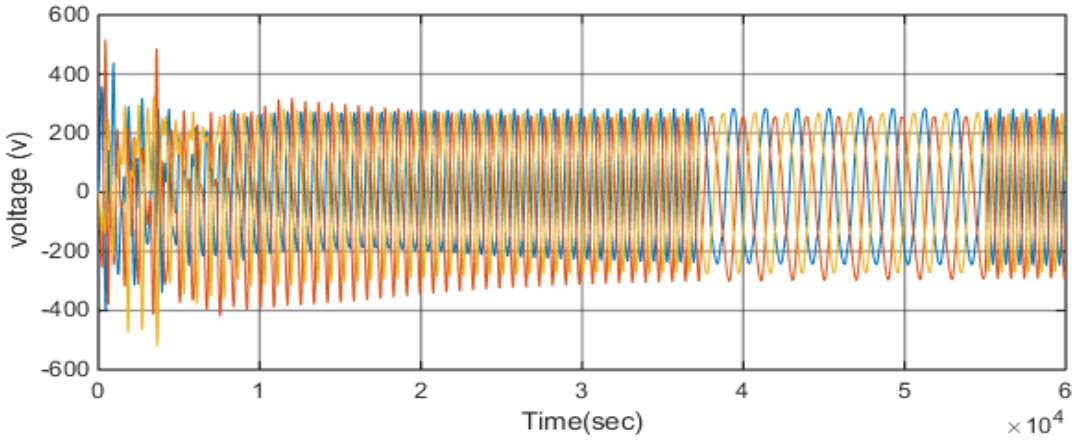

Fig.11. Voltage diagrams

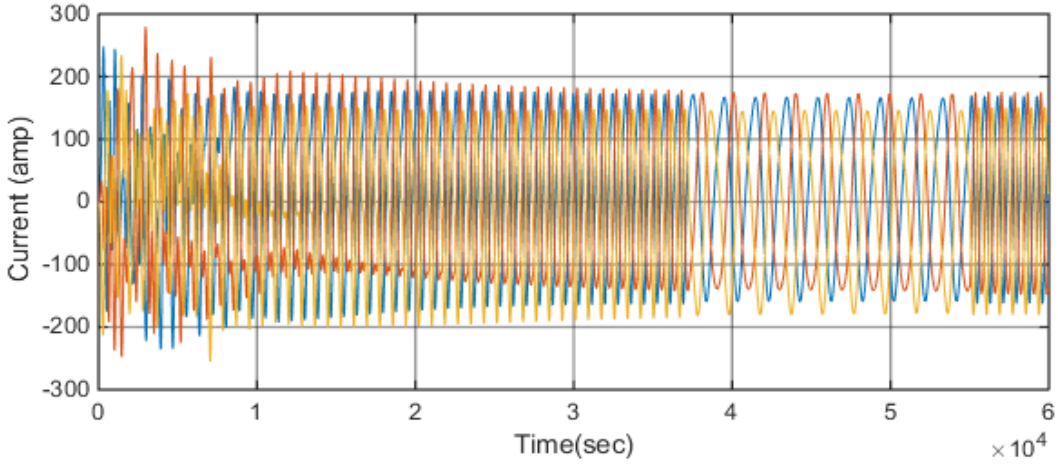

Fig. 12. Current diagrams

5.2. Optimization results

This section presents the results of optimization using the gray wolf algorithm. Considering that the gray wolf algorithm is one of the desired algorithms in the optimization process, the desired parameters in the optimization process are based on the information entered in Table 1. To evaluate the performance of the proposed control optimization strategy, the microgrid model was objectified for state transition and sudden load change simulation under the MATLAB/Simulink environment. In Figure 13, the graph shows the value of the cost function per 100 iterations performed in the optimization process. As it is known, the value of the process cost function is reduced and finally fixed to a minimum value. This shows the successful performance of the optimization algorithm.

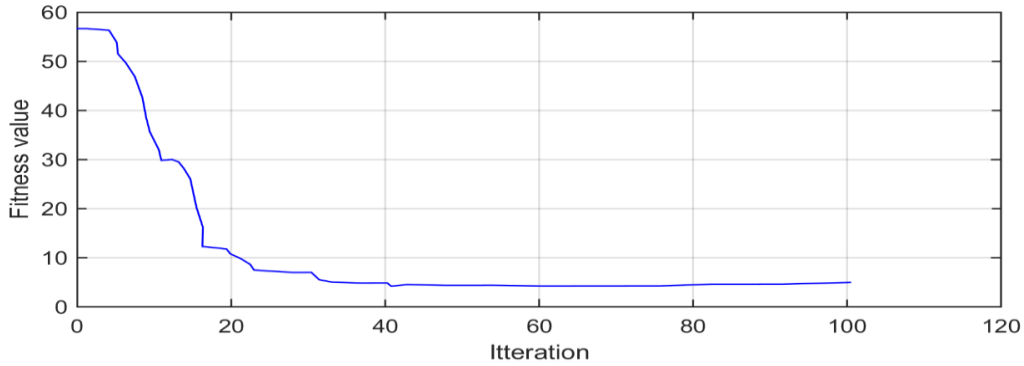

Fig.13. Value of the cost

According to the optimization process, the optimal parameters for each parameter have been calculated separately, and the optimal parameters are shown in Table 1.

Table 1. Optimal value of parameters

Parameter	Optimal value
m_p	$1e-5$
n_q	$2.9e-4$
k_{ic}	10
k_{pu}	10.15

5.3. The results of microgrid stability analysis

The small signal model extracted in the previous sections analyses the system's stability. In this order, at first, the closed-loop model is extracted for the system based on the small signal model, and then the system's stability is investigated based on the eigenvalues of its state space model. For this purpose, the closed-loop model of the defined system is considered and simulated in a MATLAB coding environment. In the next step, the eigenvalues of this closed-loop system are extracted and drawn to check the position and location of the system's eigenvalues in the complex plane.

Note that at this stage, the main goal of stability analysis is to check the system's stability in the presence of the designed controller and the applied optimization algorithms. In other words, the optimal coefficients extracted by the optimization algorithm are applied to the system and the system is analyzed in the presence of controllers and their optimal parameters. Figure 14 shows the location of the eigenvalues of the closed loop system in the presence of optimal controllers.

As shown in Figure 14, all the eigenvalues of the closed-loop system in the presence of optimal controllers have a negative real part. Therefore, it can be understood from this diagram that the optimal parameters extracted by the optimization algorithm and the controllers set with these optimal parameters make the closed loop system completely stable and perform well. In addition, as it is clear from the previous figures, this optimal control loop has kept the system stable and the whole system's frequency at the desired frequency, i.e., 60 Hz.

As it is clear from the simulation results, the optimal droop control method is able to protect the microgrid against frequency changes caused by load changes. In other words, when the load of consumers changes, it causes instability in the microgrid, especially frequency instability. However, the desired droop control method returns the network to a stable state in which the microgrid frequency remains constant at the level determined by the main network. The desired Dorp control coefficients have been well optimized using the optimization method presented in this article, making the microgrid always stable. As shown by the stability analysis results of the microgrid small signal model, the desired optimal method guarantees the system's stability well.

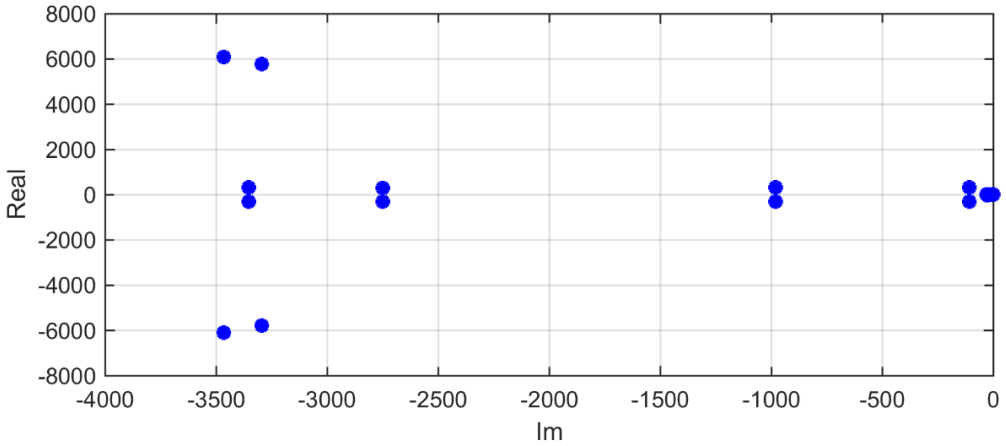

Fig. 14. Eigenvalues of the closed-loop system

6. Conclusion

To solve the problem of dynamic response in microgrid operation mode switching, this research developed an accurate small signal space state model of a microgrid based on droop control strategy, including inverter dynamics, grid dynamics and load, and then combined with a joint model. The simulation results in MATLAB/Simulink confirm the validity of the four parameters obtained from the small signal analysis that have key effects on the stability and dynamic performance under load disturbances and show the effectiveness of the proposed gray wolf approach that improves the dynamic performance of the microgrid. As a result, the proposed

control optimization scheme significantly helps to maintain microgrid stability and low voltage grid parameter selection. Using the optimal parameters obtained by the controller optimization algorithm using the gray wolf algorithm, it is determined that the closed loop system becomes completely stable, and the optimal control loop keeps the system stable and the frequency of the entire system at the desired frequency, i.e., 60 Hz. The performance of the control system was investigated in different operational situations, and the results of this investigation prove the optimal effectiveness of the proposed algorithm. This control system significantly improved the microgrid's performance by reducing the convergence time, power fluctuations and current fault tracking, especially in the higher penetration mode of DGs. The results show that the optimal control method presented in this article can protect the microgrid against frequency changes caused by load changes and fluctuations as much as 10 Amp for load current. The parameters and coefficients of the controllers of the desired control method in this article have been optimized to increase its performance as much as possible. Also, by using this control system, unwanted harmonics were significantly reduced. Also, the nature of the proposed control system ensures proper operation of DG units in large microgrids.

COMPETING OF INTERESTS

The authors declare no competing interests.

AUTHORSHIP CONTRIBUTION STATEMENT

Zhi Yuan: Writing-Original draft preparation, Conceptualization, Supervision, Project administration.

Ji Li: Methodology, Software, Validation.

DATA AVAILABILITY STATEMENT

Some or all data, models, or codes that support the findings of this study are available from the corresponding author upon reasonable request.

ACKNOWLEDGEMENT

This research was supported by the Major Science and Technology Projects in Xinjiang Uygur Autonomous Region (2022A01004-1).

REFERENCES

[1] T. L. Vandoorn, J. C. Vasquez, J. De Kooning, J. M. Guerrero, and L. Vandevelde, “Microgrids: Hierarchical control and an overview of the control and reserve management strategies,” IEEE industrial electronics magazine, vol. 7, no. 4, pp. 42–55, 2013.

[2] N. Hatziargyriou, H. Asano, R. Iravani, and C. Marnay, “Microgrids,” IEEE power and energy magazine, vol. 5, no. 4, pp. 78–94, 2007.

[3] A. Ipakchi and F. Albuyeh, “Grid of the future,” IEEE power and energy magazine, vol. 7, no. 2, pp. 52–62, 2009.

[4] A. G. Tsikalakis and N. D. Hatziargyriou, “Centralized control for optimizing microgrids operation,” in 2011 IEEE power and energy society general meeting, IEEE, 2011, pp. 1–8.

[5] R. Yuan, Q. Ai, and X. He, “Research on dynamic load modelling based on power quality monitoring system,” IET Generation, Transmission & Distribution, vol. 7, no. 1, pp. 46–51, 2013.

[6] Y. Li and Y. W. Li, “Power management of inverter interfaced autonomous microgrid based on virtual frequency-voltage frame,” IEEE Trans Smart Grid, vol. 2, no. 1, pp. 30–40, 2011.

[7] N. Pogaku, M. Prodanovic, and T. C. Green, “Modeling, analysis and testing of autonomous operation of an inverter-based microgrid,” IEEE Trans Power Electron, vol. 22, no. 2, pp. 613–625, 2007.

[8] Z. Xiao, C. Wang, and S. Wang, “Small-signal stability analysis of microgrid containing multiple micro sources,” Automation of Electric Power Systems, vol. 33, no. 6, pp. 81–85, 2009.

[9] F. Katiraei, M. R. Iravani, and P. W. Lehn, “Small-signal dynamic model of a micro-grid including conventional and electronically interfaced distributed resources,” IET generation, transmission & distribution, vol. 1, no. 3, pp. 369–378, 2007.

[10] M. A. Hassan and M. A. Abido, “Optimal design of microgrids in autonomous and grid-connected modes using particle swarm optimization,” IEEE Trans Power Electron, vol. 26, no. 3, pp. 755–769, 2010.

[11] I.-Y. Chung, W. Liu, D. A. Cartes, E. G. Collins, and S.-I. Moon, “Control methods of inverter-interfaced distributed generators in a microgrid system,” IEEE Trans Ind Appl, vol. 46, no. 3, pp. 1078–1088, 2010.

[12] Y. A.-R. I. Mohamed and E. F. El-Saadany, “Adaptive decentralized droop controller to preserve power sharing stability of paralleled inverters in distributed generation microgrids,” IEEE Trans Power Electron, vol. 23, no. 6, pp. 2806–2816, 2008.

[13] E. Barklund, N. Pogaku, M. Prodanovic, C. Hernandez-Aramburo, and T. C. Green, “Energy management in autonomous microgrid using stability-constrained droop control of inverters,” IEEE Trans Power Electron, vol. 23, no. 5, pp. 2346–2352, 2008.

[14] T. Dragičević, J. M. Guerrero, J. C. Vasquez, and D. Škrlec, “Supervisory control of an adaptive-droop regulated DC microgrid with battery

management capability," IEEE Trans Power Electron, vol. 29, no. 2, pp. 695–706, 2013.
[15] S. Augustine, M. K. Mishra, and N. Lakshminarasamma, "Adaptive droop control strategy for load sharing and circulating current minimization in low-voltage standalone DC microgrid," IEEE Trans Sustain Energy, vol. 6, no. 1, pp. 132–141, 2014.
[16] L. Meng, T. Dragicevic, J. C. Vasquez, and J. M. Guerrero, "Tertiary and secondary control levels for efficiency optimization and system damping in droop controlled DC–DC converters," IEEE Trans Smart Grid, vol. 6, no. 6, pp. 2615–2626, 2015.
[17] W. Yao, M. Chen, J. Matas, J. M. Guerrero, and Z.-M. Qian, "Design and analysis of the droop control method for parallel inverters considering the impact of the complex impedance on the power sharing," IEEE Transactions on Industrial Electronics, vol. 58, no. 2, pp. 576–588, 2010.
[18] J. Hu, J. Zhu, D. G. Dorrell, and J. M. Guerrero, "Virtual flux droop method—A new control strategy of inverters in microgrids," IEEE Trans Power Electron, vol. 29, no. 9, pp. 4704–4711, 2013.
[19] B. V Solanki, C. A. Cañizares, and K. Bhattacharya, "Practical energy management systems for isolated microgrids," IEEE Trans Smart Grid, vol. 10, no. 5, pp. 4762–4775, 2018.
[20] H. A. Muqeet, H. M. Munir, H. Javed, M. Shahzad, M. Jamil, and J. M. Guerrero, "An Energy Management System of Campus Microgrids: State-of-the-Art Literature Review. Energies 2021, 14, 6525." s Note: MDPI stays neutral with regard to jurisdictional claims in ..., 2021.
[21] R. Majumder, A. Ghosh, G. Ledwich, and F. Zare, "Operation and control of single phase microsources in a utility connected grid," in 2009 IEEE Power & Energy Society General Meeting, IEEE, 2009, pp. 1–7.
[22] D. Espín-Sarzosa, R. Palma-Behnke, and O. Núñez-Mata, "Energy management systems for microgrids: Main existing trends in centralized control architectures," Energies (Basel), vol. 13, no. 3, p. 547, 2020.
[23] A. M. Abdulmohsen and W. A. Omran, "Active/reactive power management in islanded microgrids via multi-agent systems," International Journal of Electrical Power & Energy Systems, vol. 135, p. 107551, 2022.
[24] M. M. U. Rashid et al., "Home Energy Management for Community Microgrids Using Optimal Power Sharing Algorithm. Energies 2021, 14, 1060." s Note: MDPI stays neutral with regard to jurisdictional claims in published ..., 2021.
[25] K. Matharani and H. Jariwala, "Stability analysis of microgrid with passive, active, and dynamic load," Journal of Operation and Automation in Power Engineering, vol. 11, no. 4, pp. 295–306, 2023.
[26] A. U. Krismanto, N. Mithulananthan, R. Shah, H. Setiadi, and M. R. Islam, "Small-Signal Stability and Resonance Perspectives in Microgrid: A Review," Energies (Basel), vol. 16, no. 3, p. 1017, 2023.
[27] Q. Sun, B. Wang, X. Feng, and S. Hu, "Small-signal stability and robustness analysis for microgrids under time-constrained DoS attacks and a mitigation adaptive secondary control method," Science China Information Sciences, vol. 65, no. 6, p. 162202, 2022.
[28] J.-S. Wang and S.-X. Li, "An improved grey wolf optimizer based on differential evolution and elimination mechanism," Sci Rep, vol. 9, no. 1, p. 7181, 2019.